JOURNAL OF PETROLEUM GEOMECHANICS
(JPG)

Original article

Numerical investigation of the effects of Fluid Inertia on Sand Production in Cased-Perforated Oil Wells

Hasan Ghasemzadeh[1], Ahmad Ali Khodaei Ardabili[2*]

1- Associate professor, Faculty of civil engineering, K. N. Toosi University of Technology, Tehran, Iran
2- MSc of geotechnical engineering, Faculty of civil engineering, K. N. Toosi University of Technology, Tehran, Iran

Received: 5 April 2023; Accepted: 22 July 2023

DOI: 10.22107/JPG.2023.389467.1191

Keywords

Sand production,
Fluid inertia effects,
Forchheimer's law,
Perforated completion,
Finite element method,
Helical symmetry.

Abstract

Sand production by eroding downhole and surface equipment, production loss, and some other impacts can greatly increase hydrocarbon recovery and operational costs. Prediction of sand production in oil wells is generally conducted by using linear Darcy's law as the constitutive equation for oil flow. This simple law does not include the contribution of fluid inertial in pressure drop and therefore is valid when the flow velocity is low. In petroleum engineering, deviation from Darcian trend is ordinarily considered important for gas wells, however in a perforated oil well considerable flow convergence occurs near the perforation tunnels, which makes it susceptible to inertia effects. In this paper, impacts of flow inertia on sand production from vertical cased-and-perforated oil wells are numerically analyzed. In this regard, 3D coupled, poro-elastoplastic finite element methods with arbitrary Lagrangian-Eulerian adaptive mesh approach are employed. Forchheimer's law is utilized to account for high velocity flow effects in the analysis. A pressure gradient-based erosion law is adapted for use as the sanding criterion. The helical symmetry of the perforations, generally the case in practice, is utilized to achieve a more realistic but efficient simulation. Sanding response modifications due to inertia effects are presented for the considered range of parameters. The results indicate that high velocity flow leads to an increase in hydrodynamic forces around the perforation tunnels, which in turn can lead to more sand production. It is shown that ignoring the effects of inertia in perforated oil wells can lead to significantly lower predictions of both amount and rate of sand production.

1. Introduction

Modeling of fluid flow through porous media was initiated by Henry Darcy in the mid-19th century with introducing an empirical equation between the flow velocity and piezometric head gradient. In Darcy's equation, inertia effects are ignored and this relation is valid for flow regimes with low Reynolds numbers. Darcy's equation is commonly believed to be valid as long as the Reynolds number is within the range of 1 to 10 [1].

Contribution to the pressure drop caused by inertial forces is the result of acceleration and deceleration of the fluid particles during successive changes in the path and cross section of flow [2]. In order to address the effects of high velocities, a commonly accepted approach is to use Forchheimer's equation [3] instead of Darcy's law.

Popular belief in the oil industry is that inertia effects for oil wells are insignificant and can be neglected ([4, 5]). However, some authors have confirmed the presence of high velocity flow in oil wells. Fetkovich (1973) [6] by means of a comprehensive field study of 40 oil wells, showed that the deviation from Darcy's equation is not restricted to gas wells, but that it is also relevant to oil wells in high-permeability reservoirs. Nguyen (1986) [7] conducted several

* **Corresponding Author:** khodaie@dena.kntu.ac.ir

experimental tests on perforated cores and discovered that applying Darcy's law to express fluid flow through perforation tunnels results in over-prediction of the productivity by as much as 100 percent. Settari et al. (2002) [5] demonstrated that the effects of high velocity flow can be significant for oil flow in high permeability formations having limited perforations. Al-Otaibi and Wu (2011) [8] concluded that increasing the production rate, in contrast to the predictions of Darcy's law, can lead to a nonlinear increase in pressure drop, especially for high production rates. Li et al. (2022) [9] using MRT (multiple-rate test) data in a field with highly connected and densely distributed fractures and karst, confirmed that modeling non-Darcy flow is necessary to solve the issues of history matching BHP (bottom hole pressure), high/low-rate tests and build-up pressure trends.

In the oil and gas industry, the term sand production refers to the process of co-production of individual sand grains or detached sand clumps together with formation fluids. Sand production by eroding downhole and surface equipment, production loss, and other environmental impacts can greatly increase production costs. Prevention of sand production is usually very costly and often, an acceptable sand rate determines for oil wells. If the rate of sand production remains within this limit, catastrophic sanding and failure of the wellbore will not occur. Accordingly, accurate prediction of sand production rate is of great importance to reservoir engineering. The effects of non-Darcy flow may increase the pressure gradients and seepage forces in some regions around the perforation tunnel, which in turn can result in a higher rate of sand production.

Forchheimer's equation has been used in a few studies instead of Darcy's law in the sanding analysis of oil wells. Morita et al. (1989) [10] included inertia effects in their study to realistically simulate fluid flow. Vardoulakis et al. (1996) [11] suggested that if the Reynolds number of flow reach values of order 1, sanding computations at large times should be based on Forchheimer's equation rather than on Darcy's law. Skjaerstein et al. (1997) [12], found that Forchheimer's extension of Darcy's law leads to better matching between the results of theoretical models and experimental data of sand production tests. Wang et al. (2019) [13] employed a general 3-D sand production model in their study and concluded that at high fluid flow velocities, non-Darcy effects play an important role in the sanding rate but less of a role in determining the onset of sanding.

The above-mentioned studies were either dedicated to the simple open hole completion or the effects of inertia on sand production response were not examined quantitatively. In this paper, effects of fluid inertia on sand production from vertical cased-and-perforated oil wells are numerically investigated. For this purpose, Forchheimer's law is used as the constitutive equation for fluid flow and an erosion law based on hydrodynamic forces acting on solid particles is employed as the sanding criterion.

2. Model Description

In the present study, a vertical-cased-and-perforated oil well with helically (spirally) distributed perforation tunnels around the wellbore was modeled in 3D by using a finite element program. Schematic geometry of a perforated completion is shown in Fig. 1.

Among the various parameters of the model, perforation tunnel length, formation permeability, and reservoir pressure drawdown are considered to be varied over some practical ranges. For the sake of simplicity, damages around the wellbore and the perforation tunnels resulting from drilling and perforating processes were not considered in this paper.

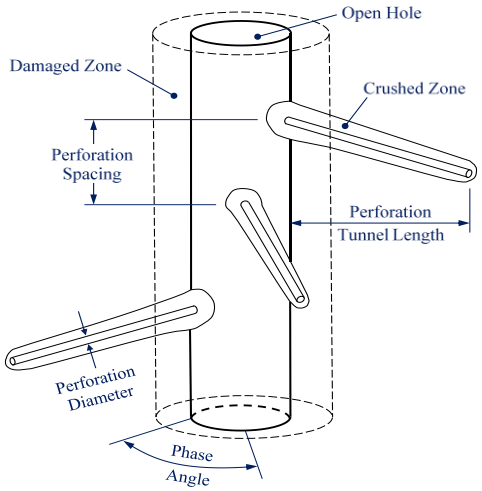

Fig. 1. Schematic view of a perforated well

2.1. Main assumptions of the model

This study focuses on a perforated completion with charge density of 6 shots-per-foot (SPF) and

angular phasing of 60°, because they are often used in practice on oil fields ([14]). Perforation tunnels are considered to be distributed helically around the borehole. In addition to the arrangement of perforations, it is assumed that materials properties and in-situ stresses have the same pattern of distribution around the wellbore. The perforated interval is assumed to be long enough to ignore end effects. With these assumptions, it is reasonable to expect that distribution of pore pressure and stresses around the wellbore, resemble the same symmetrical pattern of the perforations. For the case under consideration, typical iso-pore pressure surfaces are shown in Fig. 2. In this figure, the repeating pattern between each perforation tunnel can readily be recognizable.

Having made these assumptions, instead of modeling too many perforation tunnels, it is just required that a layer containing one perforation tunnel be explicitly modeled and analysed, provided that appropriate periodic boundary conditions be applied to the representative unit cell ([15]).

2.2. Geometry and mesh definition

The computational domain of a perforated well considered in this study is depicted in Fig. 3. As depicted in this figure, the formation is presented as a cylindrical layer containing both the wellbore and a perforation tunnel. At the top and bottom of the formation layer, some regions of non-porous material are added. These regions were included to allow the redistribution of stresses around the perforation tunnel be evolve without reaching any boundary of the model. Thickness of 5.08 cm (2 *in*) is considered for these non-porous regions.

The outer radius of the model is 1.9 *m*. Numerical evaluations showed that this value is sufficiently distant from the wellbore to ensure radial flow development at the far boundary. The borehole radius measured from the interface between cement and the formation is assumed to be 8.89 *cm* (3.5 *in*). The radius of the perforation tunnel is 7.6 *mm* (0.3 *in*) and the length of the perforation tunnel is taken as equal to 0.15, 0.23, 0.3, and 0.38 *m* (6, 9, 12, and 15 *in*).

In order to reduce the computational burden of the model, translational degrees of freedom were activated only for a 60° wide cylindrical sector which surrounds the perforation tunnel, and the rest of the model was considered as a rigid porous body (see Fig. 3b).

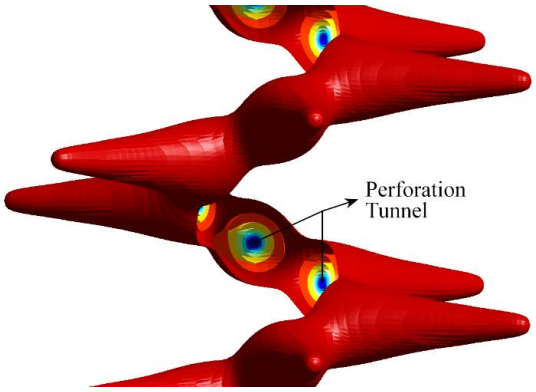

Fig. 2. Typical plot of iso-pore pressure surfaces around a perforated well with 60° phasing (warm colors represent surfaces with higher pore pressure)

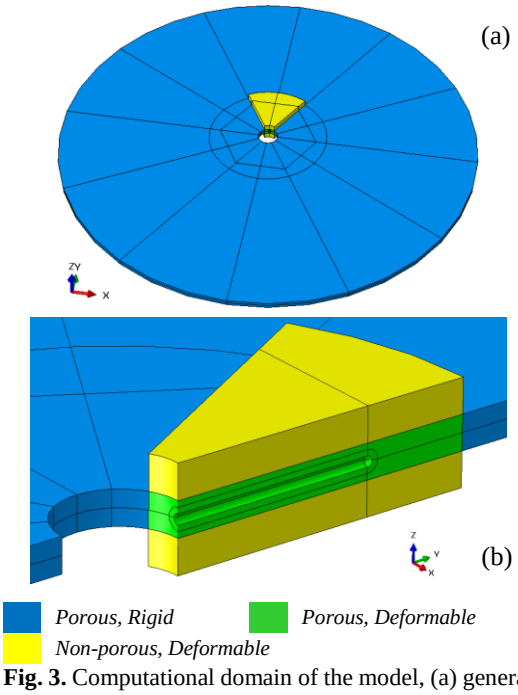

Fig. 3. Computational domain of the model, (a) general view of the model, (b) vertical section of near-wellbore region

The finite element mesh of the model was established in such a way to achieve a reasonable compromise between the accuracy of results and the expense of computations. Two types of linear three-dimensional elements were employed to build the mesh; C3D8P (8-node brick element with trilinear displacement and pore pressure) was used to model the porous rock and C3D8 (8-node

linear brick element) to discretize the upper and lower non-porous layers. Typical mesh of the model is shown in Fig. 4.

Finer mesh was used near the surface of the production cavity in order to capture high gradients of stresses and pore pressure in this region. A total number of 23476, 28396, 33316, and 38236 elements were used for discretization of the models with perforation lengths equal to 0.15, 0.23, 0.3, and 0.38 *m*, respectively. Based on the sensitivity analysis, these mesh densities are enough to ensure that the changes in the completion skin factor and cumulative plastic strains will be less than 1% with further mesh refinement.

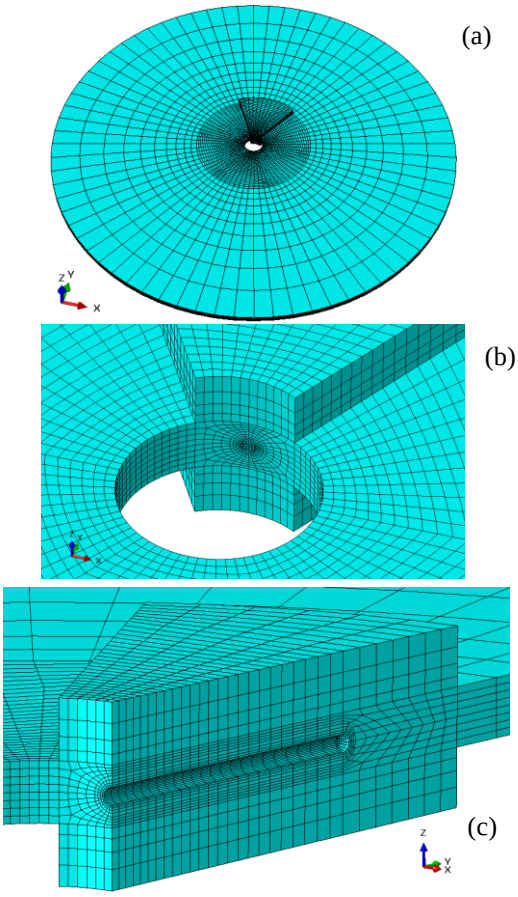

Fig. 4. Typical finite element mesh, (a) General view of the mesh (b) zoomed view of the wellbore and perforation tunnel, (c) vertical section of the near-wellbore region.

2.3. Governing equations and finite element formulation

Equations governing the transient reservoir rock–fluid interaction are the overall equilibrium relation for the rock-fluid mixture and the mass balance of the flow. These equations can be written using summation notation in the form of [16],

$$\sigma_{ij,j} - \rho\ddot{u}_i + \rho b_i = 0 \quad (1)$$

$$w_{i,i} + \alpha\dot{\varepsilon}_{ii} + \dot{p}/Q = 0 \quad (2)$$

where w_i is the average velocity of the fluid, u_i is the displacement of the solid matrix, b_i is the vector of body force per unit mass and

$$\frac{1}{Q} \cong \frac{n}{K_f} + \frac{1-n}{K_s} \quad (3)$$

$$\alpha = 1 - K_T / K_S \quad (4)$$

$$\rho = n\rho_f + (1-n)\rho_S \quad (5)$$

In the above, K_S is the average material bulk modulus of the solid components of the skeleton, K_f is the bulk modulus of the pore fluid, K_T is the average bulk modulus of the solid skeleton, ρ_f and ρ_S are the density of the fluid and solid particles, respectively and n is the porosity.

σ_{ij} in eq. 1 is the total stress tensor and can be written in terms of effective stress tensor and pore fluid pressures by Terzaghi equation (taking tensile components of stress as positive) as [16],

$$\sigma_{ij} = \sigma'_{ij} - m_{ij}\, p \quad (6)$$

where m_{ij} is the identity tensor.

The above set of equations coupled with rock and fluid constitutive equations have been solved by using the finite element method. The overall discrete equilibrium equation for the porous rock-fluid mixture in the static condition can be written in the form of [16],

$$\int_{\Omega} \mathbf{B}^T \boldsymbol{\sigma} d\Omega = \mathbf{f} \quad (7)$$

where the matrix **B** contains derivatives of the shape function (**N**), and the vector **f** contains all the effects of body forces and applied boundary tractions (**t**), i.e.

$$\mathbf{f} = \int_{\Omega} N^T \rho \mathbf{b} d\Omega + \int_{\Gamma} N^T \mathbf{t} d\Gamma \quad (8)$$

2.4. Constitutive behavior of the pore fluid and reservoir rock

Darcy's equation for single phase fluid flow through porous media neglecting gravity effects is written as ([17]),

$$-\nabla p = \mu \boldsymbol{\kappa}^{-1} \mathbf{u} \quad (9)$$

where **u** is the vector of apparent velocity of the pore fluid, p is the pore fluid pressure, $\boldsymbol{\kappa}$ is the absolute permeability tensor of the porous media with the dimension of length squared, μ is the dynamic viscosity of the fluid, γ is the specific gravity of the wetting phase, and ∇ is the gradient operator.

Forchheimer [3] added a nonlinear term to Darcy's law and introduced a new empirical equation for the conservation of one-dimensional fluid momentum along the x-axis as,

$$-\frac{\partial p}{\partial x}=\frac{\mu}{\kappa}u+\beta\rho_f u^2 \tag{10}$$

where ρ_f is the density of the fluid and β is the Forchheimer coefficient.

In this study, the correlation developed by Firoozabadi and Katz (1979) [18] is employed to determine the Forchheimer coefficient,

$$\beta=2.73\times10^{10}/\kappa^{1.1045} \tag{11}$$

where κ is expressed in *md* and β in ft^{-1}.

The permeability of a reservoir rock can be assumed to be a function of porosity. In the present study, the Carman–Kozeny law was used to express this dependency as,

$$\kappa\propto e^3/(1+e) \tag{12}$$

where e is the void ratio.

The elastoplastic behavior of the reservoir rock is expressed using the Mohr-Coulomb model due to its generality in engineering. This model represents a linear relation between the shear strength of a material with its normal stress. The Mohr-Coulomb yield criterion can be expressed as [19, 20],

$$Rq-\sigma'_m\tan\phi-c=0 \tag{13}$$

where

$$R=\frac{1}{\sqrt{3}\cos\varphi}\sin(\theta,\frac{\pi}{3})+\frac{\tan\varphi}{3}\cos(\theta,\frac{\pi}{3}) \tag{14}$$

and ϕ is the (mobilized) friction angle of the material, c is the material cohesion, σ'_m is the mean effective stress, q is the Mises equivalent stress, and θ is the deviatoric polar angle defined as [20],

$$\cos(3\theta)=(r/q)^3 \tag{15}$$

where r is the third invariant of the deviatoric stress tensor.

The yield surface evolves as plastic deformations occur. The evolution of the Mohr-Coulomb surface is described as a function of the equivalent plastic strain, which is defined by [20],

$$\bar{\boldsymbol{\varepsilon}}^{pl}=\int\frac{1}{c}\boldsymbol{\sigma}:d\boldsymbol{\varepsilon}^{pl} \tag{16}$$

where $d\boldsymbol{\varepsilon}^{pl}$ is the plastic strain increment.

The flow potential, G, for describing the plastic strains is selected as a hyperbolic function in the meridional and the smooth elliptic function in the deviatoric stress planes [20],

$$G=\sqrt{(\varepsilon c_0\tan\psi)^2+(R_w q)^2}-p\tan\psi \tag{17}$$

where

$$R_w=R\left(\frac{\pi}{3},\varphi\right)\times \tag{18}$$

$$\frac{4(1-e^2)\cos^2\theta+(2e-1)^2}{(2-2e^2)\cos\theta+(2e-1)\sqrt{(4-4e^2)\cos^2\theta+5e^2-4e}}$$

in which ψ is the dilation angle, c_0 is the initial cohesion, ε is a parameter for the meridional eccentricity, and e is a parameter for the deviatoric eccentricity which is defined by [20],

$$e=(3-\sin\varphi)/(3+\sin\varphi) \tag{19}$$

Parameters values for the constitutive behavior of the reservoir rock are reported in Table 1. The mobilized cohesion versus equivalent plastic strain is also plotted in Fig. 5. These values, adapted from [21], lie within the range of values typically used for sandstones.

Table 1. Material properties of the reservoir sandstone

Young's modulus	Poisson's ratio	Internal friction angle	Dilation angle
9.1 GPa (1.32×10^6 psi)	0.22	45°	20°

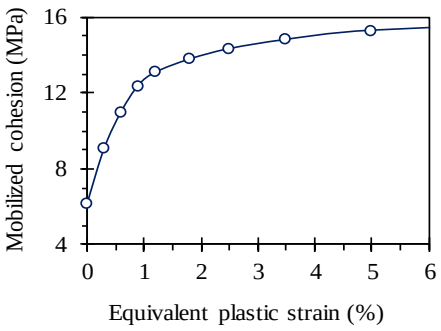

Fig. 5. Mobilized cohesion of the reservoir rock as a function of equivalent plastic strain

2.5. Initial and boundary conditions

The total overburden pressure on the perforated layer and the initial pore pressure of the reservoir are assumed to be 89.63 MPa (13000 *psi*) and 37.92 MPa (5500 *psi*), respectively. The Permeability of the reservoir is considered isotropic and values of 100, 200, and 300 *md* are employed for it. A gravity of 37° API (840 kg/m^3) is assumed for the reservoir fluid, which classifies as light crude oil. Values of other parameters used to define the initial conditions of the reservoir are given in Table 2. To simulate oil production, pore pressure on the perforation tunnel is set to a value which obtains the desired pressure drawdown. Three values of 0.69, 1.38, and 2.07 MPa (100, 200, 300 *psi*) are used as the reservoir pressure drawdowns.

After having reached the intended pressure drawdown, a transient consolidation analysis under constant pressure drawdown was performed for a time interval of 3 days, in which erosion of material due to sand production was simulated. In order to take the helical arrangement of perforation tunnels into account, periodic pressure boundary conditions are applied on the upper and lower boundaries of the porous layer.

Table 2. Initial conditions of the reservoir

Effective vertical stress	51.71 MPa (7500 *psi*)
Effective horizontal stress	34.47 MPa (5000 *psi*)
Porosity	0.26
Oil viscosity	8.0×10^{-3} Pa.s (0.8 *cp*)

2.6. Sand production criteria

Sand production is a two-stage process involving the mechanical and hydro-mechanical instabilities of the reservoir rock in the vicinity of production cavities ([11, 22]). In the first stage, drilling, completion, and production induced stresses lead to weakening and degradation of reservoir rock. Sand production occurs once the hydrodynamic forces induced by fluid flow exceed the resistance forces between sand particles or chunks and transport them to the wellbore. The total hydrodynamic force, $\mathbf{F}_{hd}$, exerted by the fluid on the unit volume of the porous media can be written as [1],

$$\mathbf{F}_{hd} = -\nabla p \tag{20}$$

In the pressure gradient-based erosion law, employed as the sanding criterion, the rate of sand production is proportional to the magnitude of hydrodynamic force [23],

$$\dot{m}/\rho_s = \lambda \|\nabla p\| \tag{21}$$

where $\dot{m}$ is the rate of solids mass produced per unit volume, λ is the sand production coefficient with a dimension of length squared times time over mass and can be determined experimentally, ρ_s is the solid density, and $\|\ \|$ denotes the norm of a vector.

By substituting the pressure gradient from equation 10 into equation 21, the sand production criterion can be rewritten in a more applicable form as,

$$\frac{\dot{m}}{\rho_s} = \lambda\left(\frac{\mu}{\kappa} + \beta\rho_f \|\mathbf{u}\|\right)\|\mathbf{u}\| \tag{22}$$

In this study, the following simple equation is used to determine λ,

$$\lambda = \begin{cases} 0 & \bar{\varepsilon}^{pl} \le \bar{\varepsilon}_c^{pl} \\ \lambda_1 & otherwise \end{cases} \tag{23}$$

where $\bar{\varepsilon}_c^{pl}$ is the threshold value of equivalent plastic strain for the onset of sand production, and λ_1 is a parameter that controls the rate of sand production.

The erosion of materials at an external boundary can be expressed by declaring the boundary to be part of an adaptive mesh zone and prescribing the recession velocity of the boundary mesh into the material. In this technique, subsurface nodes are adjusted to account for erosive material loss. Within this framework, $\dot{m}$ term on the left-hand side of equation 21 represents the rate of solids mass produced per unit boundary surface.

3. Results and Discussion

3.1. Hydrodynamic force evolution

For ease of presentation, a baseline case with input parameters given in Table 3 is defined. The baseline case includes two different quantities for the β factor which are addressing the linear and nonlinear flow equations.

Using the Karakas-Tariq model [24], a skin factor of -0.25 obtains for the baseline case. Having estimated the skin factor, the flow rate of well per each perforation tunnel can be calculated as [4],

$$q_p = \frac{2\pi\kappa_h h(p_{res} - p_w)}{\mu\ln\left[(r_e/r_w) + s\right]} \tag{24}$$

where q_p is the flow rate per each perforation, h is the spacing between two successive perforations,

s is the skin factor and r_w and r_e are the wellbore and drainage radius, respectively. Numerical simulation yields the flow rate of 3.23 m^3/d (20.35 bbl/d) which is in good accordance with 3.31 m^3/d (20.95 bbl/d) obtained by equation. 24.

For the baseline case with $\beta = 0$, contour and iso-surface plots of the pore pressure around the perforation tunnel are shown in Fig. 6. In this figure, flow convergence into the explicitly modeled perforation tunnel and its adjacent tunnels indicates the proper functioning of the periodic boundary conditions.

Table 3. Input parameters for the baseline case

Parameter		Value	
		SI Unit	Oilfield Unit
Wellbore radius	r_w	0.0889 *m*	0.29 *ft* (3.5 *in*)
Perforation length	L_p	0.15 *m*	0.5 *ft* (6 *in*)
Perforation Radius	r_p	7.62 *mm*	0.025 *ft* (0.3 *in*)
Shot Phasing angle	φ	60°	60°
Formation Permeability	κ	1.974×10^{-13} m^2	200 *md*
Forchheimer coef.	β	0, 1.645×10^{8} m^{-1}	0, 5.014×10^{7} ft^{-1}
Pressure drawdown	Δp_{dd}	1.38 MPa	200 *psi*

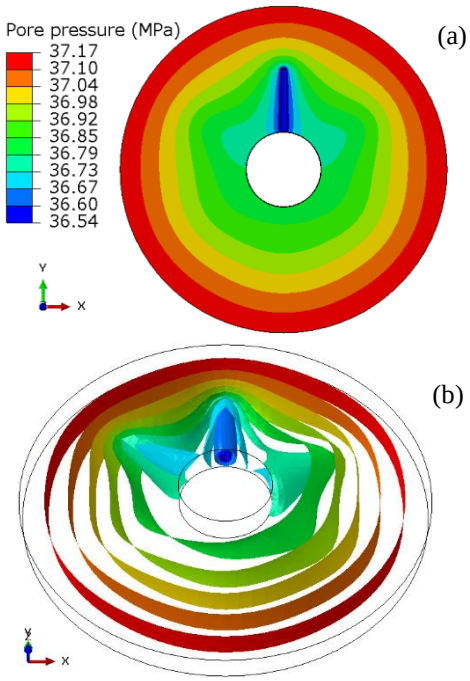

Fig. 6. Pore pressure distribution for the baseline case with $\beta = 0$, (a) pressure contour at a horizontal plane, crossing the perforation axis, (b) iso-pressure surfaces

For the baseline case with and without inertia effects, contours of fluid velocity around the perforation tunnel are shown in Fig. 7. As illustrated in this figure, maximum fluid velocity using Darcy's law obtains as 12.4 *mm*/*s*, which reduces to 10.34 *mm*/*s* by considering inertial effects. According to this figure, inertia effects mainly affect the fluid velocity in the vicinity of perforation tip.

Contours of the hydrodynamic force for the baseline case are shown in Fig. 8. This figure demonstrates that for both linear and nonlinear flow, the perforation tip is the zone of the highest seepage forces. Maximum hydrodynamic force per unit volume of porous media considering inertia effects obtains as 65.1 N/cm^3 which reduces to 50.2 N/cm^3 by ignoring these effects. This means about 23 percent underestimation of the maximum hydrodynamic force.

For all cases, the percentage of underestimation made on the hydrodynamic force at the junction of the wellbore and perforation tunnel (which is most susceptible to sand production) as a function of flow rate is depicted in Fig. 9. Maximum underestimation in this figure (29%) belongs to a short perforation in a high permeability formation with high pressure drawdown. This figure indicates that both the flow rate and length of the perforation tunnel are important parameters in the study of high velocity flow effects. It is evident that with increasing the perforation length, the error introduced by ignoring inertia effects reduces.

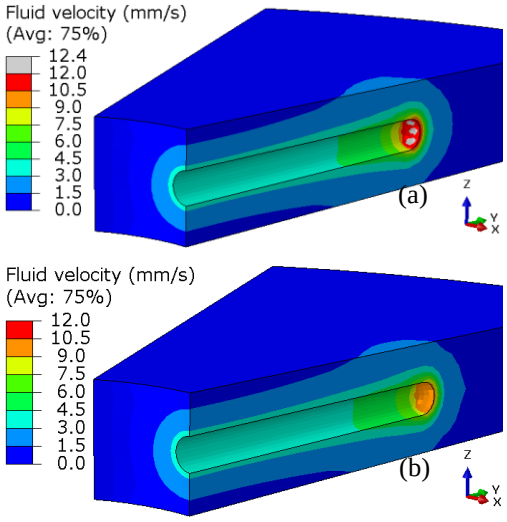

Fig. 7. Contours of fluid velocity around the perforation tunnel for the baseline case, (a) without inertia effects ($\beta = 0.0$), (b) with inertia effects

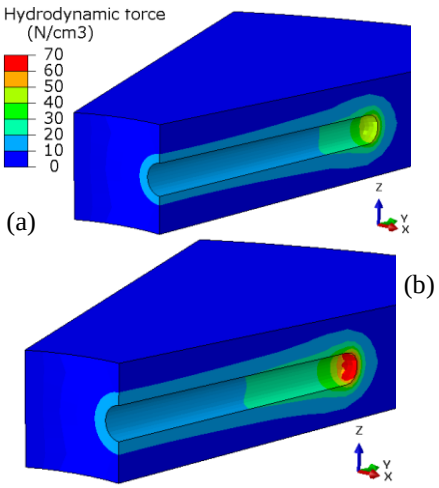

Fig. 8. Contours of hydrodynamic force per unit volume of material for the baseline case, (a) without inertia effects, (b) with inertia effects

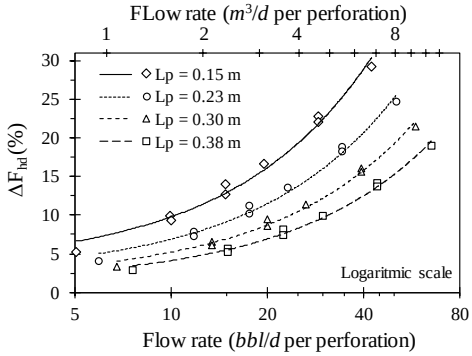

Fig. 9. Error arises on hydrodynamic force due to ignoring inertia effects at the junction of wellbore and perforation tunnel (all cases)

3.2. Distribution of plastic strains

In the previous subsection, it was shown that the effects of inertia can lead to considerable changes in hydrodynamic force around the perforation tunnel. Because the rate of sand production is proportional to hydrodynamic force, it is reasonable to expect that, inertia effects should play an important role in sand production, if be considerable in zones with high plastic strains.

The contour of equivalent plastic strain around the perforation tunnel is shown in Fig. 10. According to the figure, plastic strains have concentrated on the lateral sides of the perforation tunnel. Plastic strain is higher at the entrance of the perforation tunnel and reduces by moving toward the cavity tip. It is worth noting that, for the considered range of parameters no significant changes in plastic strain were observed due to inertia effects.

In order to investigate the effect of perforation tunnel length on the distribution of plastic strains, for a cases with input parameters as in Table 3, but with perforation lengths of 0.15 *m* and 0.3 *m*, peak equivalent plastic strain at different distances from the well face are compared in Fig. 11. This figure shows that in the both cases, the entrance of perforation tunnel has the highest plastic strain and by moving toward the cavity tip, plastic strains diminish. Also, it is evident that increasing the length of the perforation tunnel does not induce a noticeable change in zones with high plastic strains.

To ascertain the effect of pressure drawdown on plastic strain distribution around the perforation tunnel, for the baseline case, but with drawdowns of 0.69, 2.07 *MPa* (100, 300 *psi*), peak equivalent plastic strain at different distances from the well face are compared in Fig. 12. According to the figure, plastic strain increases with pressure drawdown. However, for the considered range of parameters, effective stresses on the perforation wall are by far higher than the pressure drawdown, and therefore the pressure drawdown has not significantly contributed to plastic strain.

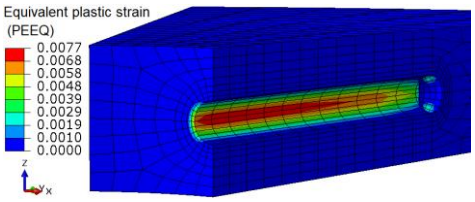

Fig. 10. Contour of equivalent plastic strain around the perforation tunnel for the baseline case with $\beta = 0$

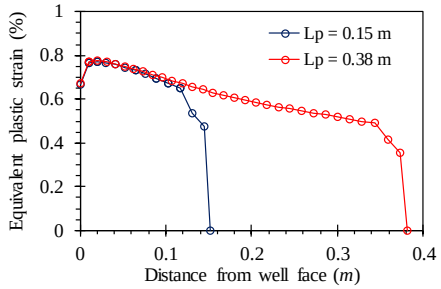

Fig. 11. Peak equivalent plastic strain at different distances from the junction of the wellbore and perforation tunnel for *Lp* = 0.15 and 0.38 *m* (other parameters as in Table 3)

Therefore, for the considered range of the parameters it does not matter how much inertia effects are high in the perforation tips and other

relatively intact zones, they can contribute to sand production if be noticeable near the junction of the perforation tunnel with the wellbore.

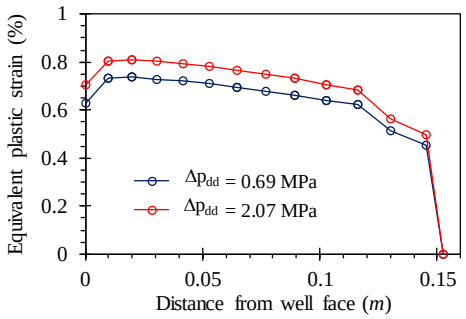

Fig. 12. Peak equivalent plastic strain at different distances from the well face for Δp_{dd} = 0.69 and 2.07 *MPa* (other parameters as in Table 3)

3.3. Sand production response

According to the employed criteria for sand production (equations 22 and 23), two factors: equivalent plastic strain and pore pressure gradient, determine the rate of sand production. The onset of sand production is dictated by the equivalent plastic strain, which was seen is almost independent of inertia effects, but increases with pressure drawdown. For each value of pressure drawdown, a specific plastic strain threshold is considered. This threshold value was kept equal to 80% of the maximum equivalent plastic strain observed after the application of pressure drawdown. The values of critical plastic strain for different drawdowns are given in Table 4.

Table 4. Critical plastic strain for onset of sand production

Pressure Drawdown (MPa), Δp_{dd}	0.69 (100 psi)	1.38 (200 psi)	2.07 (300 psi)
Critical plastic strain (%), $\bar{\varepsilon}_c^{pl}$	0.59	0.62	0.65

For all the considered cases, the sand production coefficient, λ_1, was set to 1.5×10^{-10} mm^3s/gr. The sand production analysis is run for a time period of three days to investigate the initial response of sand production.

The shape of the cavity for the baseline case after 3 days of sand production with and without inertia effects are shown in Fig. 13. It is seen that the largest amount of erosion occurred near the entrance of perforation tunnel. Further away from the junction of perforation tunnel with the wellbore, the amount of sand production progressively decreases. This behavior has been observed in laboratory studies by Fattahpour et al. (2012) [25] on perforated sandstone cores. According to this figure, the tip of perforation tunnel has not contributed to sand production, which is expected because no significant plastic strain had developed in this region. In the case under consideration, the cavity section changes from an original circular shape to an elliptical one through sand production. Papamichos et al. (2004) [26] demonstrated through experimental and numerical analysis that ellipsoid geometry is more stable than circular geometry. Thus, following the erosion of materials from plastic regions, more stable geometry is formed under the applied stresses which may slow down or cease the production of sand.

For the baseline case with and without inertia effects, the cumulative sand production versus time is plotted in Fig 14. In this figure, the effects of high velocity flow have clearly been demonstrated by increasing both the amount and rate of sand production. The amount of produced sand for the linear model is about 0.6 *gr*, which reaches 0.81 *gr* by considering inertia effects. According to this figure, the average sand rate on the last day of simulation for linear and nonlinear cases are about 0.3 *gr*/*d* and 0.4 *gr*/d, respectively which means 25% underestimation due to ignoring the effects of high velocities. It should be noted that many perforation tunnels emanate from a wellbore, and the total mass of produced sand will be the sum of that for all the perforation tunnels.

For a perforation tunnel with length of 0.38 *m* and other parameters as in Table 3, the cumulative sand mass for linear and nonlinear cases are plotted in Fig. 15. Comparison of Fig. 14 with Fig. 15 reveals that the effects of high velocity flow on sand production decrease for increasing perforation length. This behavior is expected, because it has already been shown that the hydrodynamic force also has a similar trend.

The total mass of produced sand for the whole range of parameters is shown in Fig. 16. Error arises due to ignoring inertia effects also depicted in this plot. Figures 17a and 17b show the amount of produced sand versus the length of the perforation tunnel with and without inertia effects, respectively. It is evident that both the length of the perforation tunnel and pressure drawdown have significant impacts on sand production. The figure also shows that under a constant drawdown, the effects of reservoir permeability on sand production cannot be captured without considering inertial effects. Fig. 17c shows that the underestimation due to ignoring inertia effects

increases with pressure drawdown and decreases with the length of the perforation tunnel.

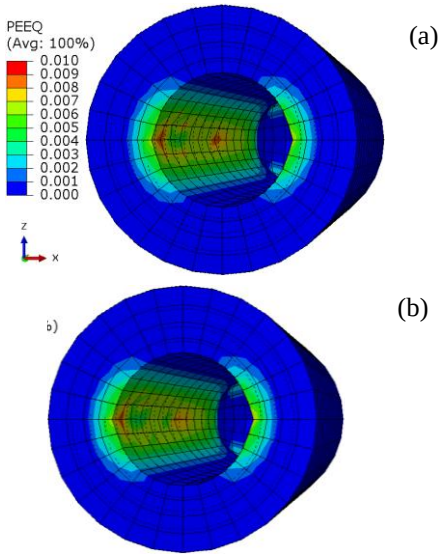

Fig. 13. Shape of the perforation tunnel after three days of sand production for the baseline case, (a) without inertia effects (β = 0), (b) with inertia effects (dashed line represents the undeformed shape)

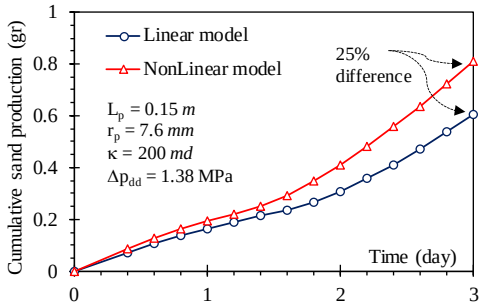

Fig. 14. Cumulative sand production from a perforation tunnel (baseline case)

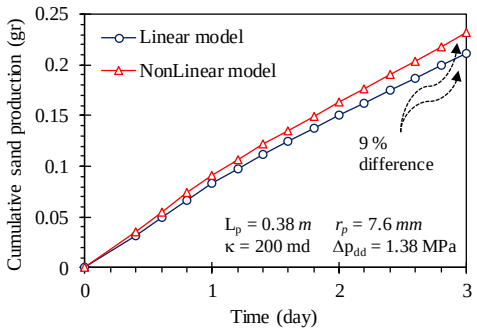

Fig. 15. Cumulative sand production from a perforation tunnel with length of 0.38 m versus time (other parameters are as in Table 3)

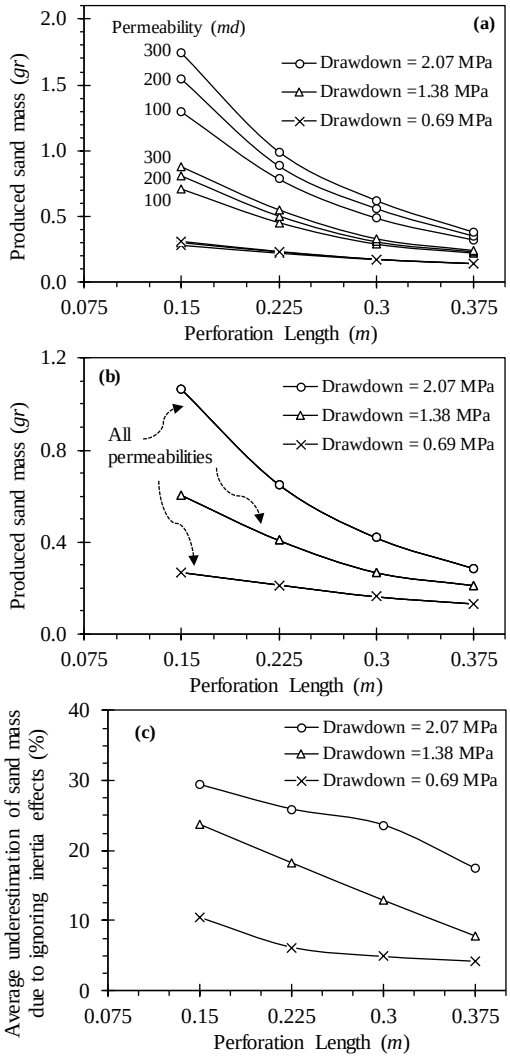

Fig. 16. Effects of drawdown and permeability on sand production, (a) total sand mass with considering inertial effects, (b) total sand mass without considering inertia effects, (c) Underestimation due to ignoring the inertia effects

For all the considered cases, the underestimation of produced sand mass due to inertia effects as a function of flow rate is shown in Fig. 17. According to this figure, for the considered range of parameters, the maximum error is about 39% which belongs to a short perforation tunnel in a high permeability formation with high pressure drawdown. The underestimation due to ignoring inertia effects increases with decreasing the length of perforation tunnel. For a specific perforation length, each of pressure drawdown and permeability which leads to an increase in flow rate also increases the

contribution of inertia effects to sand production. Therefore, knowing the flow rate of a wellbore is not enough to judge the effects of flow inertia. Other parameters such as perforation length, reservoir pressure drawdown, and permeability are important for assessing inertia effects.

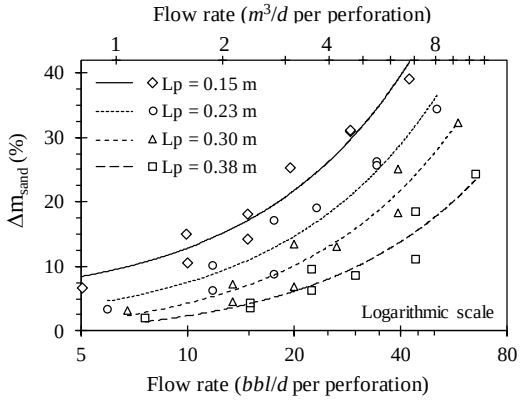

Fig. 17. Error arises on mass of produced sand due to ignoring inertia effects

It is worth noting that in order to evaluate the mesh size effects, the results of the baseline model were determined for a finer mesh density. It was observed that while the size of elements is such that the changes in both flow rate and plastic strains are less than 1%, the changes in the mass of produced sand are not significant.

4. Conclusions

In this study, the contributions of fluid inertia on sand production were numerically examined. Special attention was paid to realistic but efficient numerical simulation of perforated oil wells. In this regard, helical symmetry of perforation tunnels was utilized in the modeling. In order to express the erosion of materials, a pressure gradient law which is based on the physics of particles erosion was adapted as the sanding criteria. Based on the results, the following conclusions can be drawn:

1- The effects of fluid inertia by modifying the hydrodynamic forces around perforation tunnels can play a significant role on sand production. Ignoring these effects could be overly optimistic and leads to a lower estimate of sand production. In the considered range of parameters, maximum error on produced sand mass due to ignoring inertia effects was obtained as high as 39%, which belongs to a short perforation tunnel in a high permeability formation with high pressure drawdown.

2- By increasing the flow rate per perforation tunnel, the contribution of fluid inertia to sanding response increases. However, other parameters including perforation length, reservoir pressure drawdown, and permeability are also effective in this regard. The influence of high velocity flow on sand production varied in proportion to the pressure drawdown and inversely to the perforation length. In general, knowing the flow rate of the wellbore is not enough to judge the effects of flow inertia.

3- If the contribution of inertia effects to pressure gradient be significant in regions with high plastic strains, the effects of inertia will also significantly change the response of sand production. It was observed that, unlike the hydrodynamic force, plastic strain is higher at the junction of the perforation tunnel with the wellbore and its magnitude reduces by moving toward the perforation tip.

Numerical simulation was used to achieve the results of this paper. More experimental and numerical studies are required to fully understand the effects of inertia on sand production.

5. References

[1] Bear J. (1972), Dynamics of Fluids in Porous Media, American Elsevier Publishing Company, Dover, New York.

[2] Geertsma, J. (1974), Estimating the Coefficient of Inertial Resistance in Fluid Flow Through Porous Media, J Geophys Res-Sol Ea, 14, 445-450.

[3] Forchheimer, P. (1901), Water movement through soil, Zeitschrift des Vereines Deutscher Ingenieure, 45, 1782-1788.

[4] Dake, L.P. (1998), Fundamentals of Reservoir Engineering, 17th edn. Elsevier Science, The Hague, The Netherlands.

[5] Settari, A., Bale, A., Bachman, RC., Floisand, V. (2002), General Correlation for the Effect of Non-Darcy Flow on Productivity of Fractured Wells, Paper presented at the SPE Gas Technology Symposium, Calgary, Canada.

[6] Fetkovich M.J. (1973), The Isochronal Testing of Oil Wells, Paper presented at the Fall Meeting of the Society of Petroleum Engineers of AIME, 30 Las Vegas, Nevada.

[7] Nguyen, T.V. (1986), Experimental Study of Non-Darcy Flow Through Perforations, Paper presented at the SPE Annual Technical Conference and Exhibition, New Orleans.

[8] Al-Otaibi A., Wu Y-S. (2011), An Alternative Approach to Modeling Non-Darcy Flow for Pressure Transient Analysis in Porous and Fractured Reservoirs,

SPE/DGS Saudi Arabia Section Technical Symposium and Exhibition, Al-Khobar, Saudi Arabia.

[9] Li, D., Ionescu, C-L., Ehighebolo, I.T., Jr, B.H., Zhazbayeva, A., Yergaliyeva, B., and Francia, L. (2022 November), Modeling and Simulation of Non-Darcy or Turbulent Flow for Oil Wells, Paper presented at the SPE Annual Caspian Technical Conference, Nur-Sultan, Kazakhstan.

[10] Morita, N., Whitfill, D.L., Massie, I., Knudsen, T.W. (1989), Realistic Sand-Production Prediction: Numerical Approach, SPE Production Engineering Journal, 4, 15–24.

[11] Vardoulakis, I., Stavropoulou, M., Papanastasiou, P. (1996), Hydro-mechanical aspects of the sand production problem Transport Porous, Med 22, 225-244.

[12] Skjaerstein, A., Stavropoulou, M., Vardoulakis. I, Tronvoll. J. (1997), Hydrodynamic erosion; A potential mechanism of sand production in weak sandstones, Int J Rock Mech Min 34, 292.e1-292.e2.

[13] Wang, H., Gala., D.P, Mukul M.Sh. (2019), Effect of Fluid Type and Multiphase Flow on Sand Production in Oil and Gas Wells, SPE J. 24, 733–743.

[14] Sun, D., Li, B., Gladkikh, M., Satti, R., Evans, R. (2013), Comparison of Skin Factors for Perforated Completions Calculated with Computational-Fluid-Dynamics Software and the Karakas-Tariq Semianalytical Model, SPE Drill Completion, 28, 21-33.

[15] Sadrnejad, S.A, Ghasemzadeh, H., Khodaei Ardabili, A.A. (2018), A Finite Element Model for Simulating Flow around a Well with Helically Symmetric Perforations, Journal of Engineering Geology, 12, 159-188.

[16] Chan A.H.C., Pastor M., Schrefler B.A., Shiomi T., Zienkiewicz O.C. (2022), Computational Geomechanics Theory and Applications, 2nd eddition, John Wiley & Sons Ltd, Hoboken, USA.

[17] Aziz K., Settari A. (1979), Petroleum reservoir simulation, Applied Science Publishers, Great Britain.

[18] Firoozabadi A, Katz D.L. (1979), An Analysis of High-Velocity Gas Flow Through Porous Media, J Petrol Technol, 211-216.

[19] Potts D.M., Zdravković L. (1999), Finite Element Analysis in Geotechnical Engineering: Theory, Thomas Telford, London, England.

[20] Menetrey Ph., Willam K. J. (1995), Triaxial Failure Criterion for Concrete and its Generalization, ACI Structural Journal, 92, 311–318.

[21] Eshiet K., Sheng Y. (2013), Influence of rock failure behaviour on predictions in sand production problems, Environ Earth Sci, 70, 1339-1365.

[22] Gravanis, E., Sarris E., Papanastasiou P. (2015), Hydro-mechanical erosion models for sand production, Int J Numer Anal Met, 39, 2017-2036.

[23] Papamichos, E. (2004), Failure in rocks: Hydro-mechanical coupling for erosion Revue Française de Génie Civil, 8, 709-734.

[24] Karakas, M., Tariq, S.M. (1991), Semianalytical Productivity Models for Perforated Completions, SPE Production Engineering, 6, 73-82.

[25] Fattahpour, V., Moosavi, M., and Mehranpour, M. (2012), An experimental investigation on the effect of rock strength and perforation size on sand production, J Petrol Sci Eng, 86–87, 172-189

[26] Papamichos, E., Liolios, P., van den Hoek, P.J., (2004), Breakout Stability Experiments and Analysis. Paper presented at the Gulf Rocks 2004, the 6th North America Rock Mechanics Symposium (NARMS), Houston, Texas.